

# UW-GS: Distractor-Aware 3D Gaussian Splatting for Enhanced Underwater Scene Reconstruction

Haoran Wang, Nantheera Anantrasirichai, Fan Zhang, and David Bull  
 School of Computer Science, University of Bristol, Bristol, UK  
 {yp22378,n.anantrasirichai,fan.zhang,dave.bull}@bristol.ac.uk

## Abstract

*3D Gaussian splatting (3DGS) offers the capability to achieve real-time high quality 3D scene rendering. However, 3DGS assumes that the scene is in a clear medium environment and struggles to generate satisfactory representations in underwater scenes, where light absorption and scattering are prevalent and moving objects are involved. To overcome these, we introduce a novel Gaussian Splatting-based method, UW-GS, designed specifically for underwater applications. It introduces a color appearance that models distance-dependent color variation, employs a new physics-based density control strategy to enhance clarity for distant objects, and uses a binary motion mask to handle dynamic content. Optimized with a well-designed loss function supporting for scattering media and strengthened by pseudo-depth maps, UW-GS outperforms existing methods with PSNR gains up to 1.26dB. To fully verify the effectiveness of the model, we also developed a new underwater dataset, S-UW, with dynamic object masks. The code of UW-GS and S-UW will be released [here](#).*

## 1. Introduction

Ocean exploration has gained increasing importance in recent years, driven by the applications in underwater archaeology, geology, and other marine sciences. However, underwater activities are often constrained by the limitations of current technologies, the scarcity of diving experts, and high operational costs. As a result, 3D scene reconstruction has become crucial, as it allows underwater data to be captured, visualized, and analyzed onshore, facilitating more extensive and detailed studies without the need for continuous physical presence underwater.

The latest advances in 3D scene representations typically employ Neural Radiance Field (NeRF) [32] and 3D Gaussian Splatting (3DGS) [22] based methods to model static video content captured in the wild. NeRF models implicitly represent a scene as a radiance field parameterized by a

deep neural network that predicts volume density and colors. Although it offers effective view synthesis, training NeRF requires substantial computational time. Moreover, the implicit neural radiance fields also tend to yield suboptimal reconstruction results [14]. In contrast, 3DGS provides a faster alternative for training and rendering [6], which represents a scene using a set of points in space, referred to as “Gaussians”, and generally delivers better quality.

Despite the rapid growth of NeRFs and 3DGSs, most methods are designed for clear media, while only a few studies have attempted to reconstruct 3D scenes in diffuse environments, such as haze and underwater [34]. Underwater scenes, in particular, face highly variable lighting conditions influenced by factors such as water depth, surface waves, and water clarity. Visual content in these settings often experiences significant attenuation and degradation due to **light absorption** and **backscattering**, leading to inaccuracies in color and density estimations in the 3D reconstruction methods, especially 3DGS, as shown in the upper row **Figure 1**. Additionally, underwater scenes typically contain **moving elements**, such as fish and floating debris, increasing complexity. These elements are frequently referred to as distractors in 3D modeling because they are not consistently present and create artifacts in some viewpoints [35], as seen in **Figure 1** bottom row. To deal with them, the models must accurately differentiate between static and dynamic components, a task that becomes more challenging in a fluid medium. Unfortunately, the existing methods [26, 39] do not address this issue.

To address the aforementioned issues, we propose a new Gaussian Splatting (GS)-based method, UW-GS, specifically for underwater scenes. Unlike traditional 3DGS methods, which struggle with light scattering due to their use of spherical harmonics, our approach includes a novel color appearance model that integrates medium effects into Gaussian attributes and employs affine transformations to account for appearance variations at different distances. We also introduce a physics-based density control strategy to enhance the clarity of distant objects by ensuring an adequate Gaussian representation. To manage distractors, we

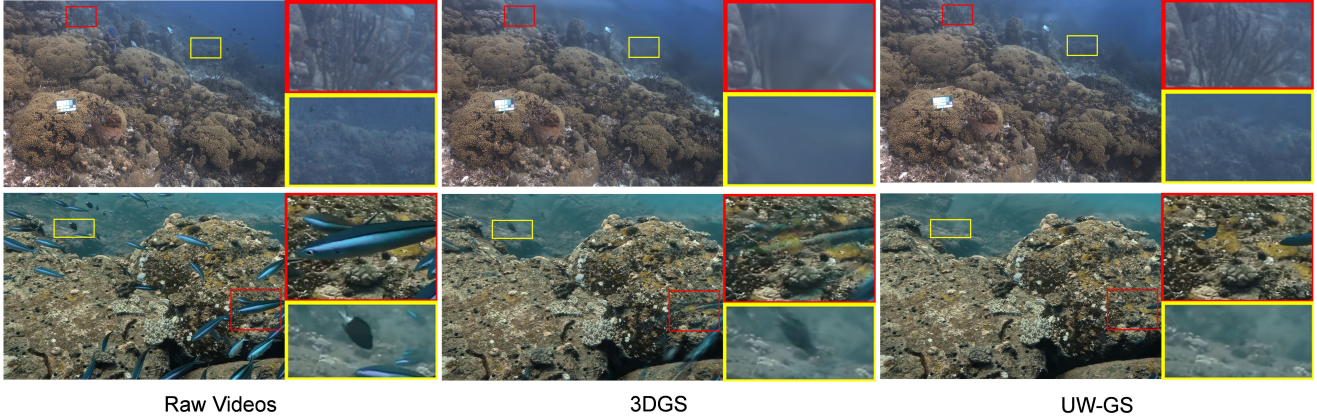


Figure 1. Visual comparison between 3DGS [22] and our proposed UW-GS method. Left to right: Raw videos and the results of 3DGS and UW-GS, respectively. The top row, enhanced for visualization purposes, shows that UW-GS produces sharper results than 3DGS. The bottom row demonstrates UW-GS’s better capability in handling moving objects.

have developed a robustness estimation algorithm for GS that utilizes a binary motion mask during rendering to minimize the impact of dynamic content on training. The proposed UW-GS is optimized using a new loss function based on the characteristics of scattering media, to reduce blurring effects and enable more accurate medium effect estimation. We also incorporated pseudo-depth maps generated from DepthAnything [47], trained with more general scenes, to enhance the robustness of our method. Finally, given the scarcity of underwater datasets, we collected a new dataset featuring four expansive areas of shallow underwater scenes, each presenting unique challenges compared to existing datasets. We also provide dynamic object masking maps in this database to facilitate further study and evaluation. In summary, our key contributions are as follows:

- 1) We, for the first time, propose a Gaussian Splatting based solution for underwater scene representation with distractor awareness, UW-GS.
- 2) UW-GS employs a novel color appearance model, transforming Gaussian colors to address low contrast and color distortion issues due to light attenuation and scattering.
- 3) We propose a new physics-based density control strategy aimed at preventing sparse Gaussians in highly absorptive and scattering media. This approach significantly enhances the clarity of details in distant areas.
- 4) We propose a new loss function that combines scattering medium characteristics with pseudo-depth maps and a pixel-wise binary motion mask to address estimated depth ambiguity and moving distractors in underwater scenes, respectively.
- 5) We introduce the first shallow underwater dataset, complete with associated distractor markers. This dataset presents unique challenges, including light flickering

and water currents, adding complexity to 3D reconstruction.

## 2. Related Work

**Underwater Imaging.** Underwater environments often suffer from issues such as color cast, image distortion, and contrast loss, largely due to the physical properties of water and its interaction with light [16]. Given the similarities between haze and underwater image processing, techniques such as the dark-channel prior [17], gray-world assumption [11], and histogram equalization [15] have been employed. Moreover, several studies have modeled underwater light behaviors, including the characterization of underwater light propagation [9], radiative transfer theory [10], and light reflectance models [9]. The Revised Underwater Image Formation Model (UIFM) [1] is currently the most widely used, noting that attenuation and backscattering factors for direct and backscattered signals differ and are thus modeled independently. Various works in underwater image processing [20, 21, 50] have achieved remarkable results using this model. However, relying solely on single-image processing can yield inconsistent results across similar scenarios, limiting the reliability and effectiveness of these approaches, particularly used for 3D modeling.

**Neural Radiance Fields (NeRFs)** [32] have significantly advanced the field of 3D reconstruction in recent years. NeRF utilizes a radiance field—a volumetric representation that calculates density and color for each sampled point along a ray [8]. Subsequent NeRF-based techniques have improved synthesis through various methods, including cone tracing instead of traditional ray tracing [3, 4], super-resolution techniques [18, 28], grid-based methods [5, 38, 41], and deblurring [42]. Moreover, more compact models using fewer parameters have been developed [45],

and faster rendering techniques have been introduced [29]. NeRF has also been extended to dynamic [30] and few-shot rendering scenarios [37]. However, these methods generally struggle in scattering media. To address this, scatterNeRF [34] was developed, effectively distinguishing objects from the medium in foggy scenes. SeaThru-NeRF [26] utilizes a novel architecture to determine water medium coefficients based on the revised underwater image formation model [1]. Moreover, other work [39] aims to accurately represent underwater scenes, incorporating dynamic rendering and tone mapping to handle variable illumination. Despite these advancements, NeRF-based methods still face challenges with the slow training and rendering times, especially in large-sized scenes.

**3D Gaussian Splatting (3DGS)** [22] is an explicit representation method that utilizes a set of trainable 3D Gaussian points. Due to its fast training speed and high-quality real-time rendering capabilities, 3DGS has become a highly popular technology in computer graphics. Leveraging these advantages, our method is also developed based on 3DGS. Numerous enhancements have been proposed to optimize this approach for challenging data. These improvements include techniques for deblurring [7, 24], anti-aliasing [46, 49], frequency regularization [51], and refined density control strategies [52]. Additionally, 3DGS has been adapted for 4D rendering [43] to accommodate dynamic scene rendering. Despite these advances, the inherent properties of 3DGS still pose limitations on its performance in complex underwater environments [27].

### 3. Method

#### 3.1. Problem formulation

3D Gaussian Splatting (3DGS) is a point-based approach that uses discrete Gaussian point clouds to represent a 3D scene. When rendering for a specific view, these 3D Gaussians are projected onto 2D space. Each Gaussian is modeled as follows:

$$G(x) = \exp\left(-\frac{1}{2}(x - \mu)^T \Sigma^{-1}(x - \mu)\right), \quad (1)$$

where  $G$  is the Gaussian function with center position  $\mu$  and 3D covariance matrix  $\Sigma$ . Each Gaussian is also characterized by opacity  $\alpha$ , view-dependent color  $c$ , expressed by spherical harmonics (SH). The  $\alpha$ -blending method is applied to generate the final image color, which is rasterized as described in Equation 2:

$$C = \sum_{i \in [1, N]} \alpha_i c_i \prod_{j=1}^{i-1} (1 - \alpha_j), \quad (2)$$

where  $N$  refers to the number of Gaussians.

During training, the 2D position gradient, an intermediate result in backward propagation, is used as evidence to indicate ‘‘color under-represented’’ issues [23]. Based on its average value, the sparse point cloud obtained from COLMAP [36] is adaptively grown by splitting and cloning. Additionally, 3DGS control the number of Gaussians through periodic pruning to prevent over-densification. However, Equation 2 is insufficient for representing the underwater scenes [39]. Unlike clear air medium, the absorption and scattering effects in underwater environments can introduce additional attenuation and backscattering, impacting the scene representation. Following the suggestion in [1], underwater image intensity can be modeled as:

$$I = J \cdot T^D + B^\infty \cdot (1 - T^B), \quad (3)$$

where  $I$  represents the camera-captured color,  $J$  is the true object color in the scene without medium effect,  $B^\infty$  denotes the background light color at the infinite distance.  $T^D$  and  $T^B$  reflect the impact of the medium (water) on the light coming directly from the object and the light that is backscattered by the water, respectively:

$$\begin{aligned} T^D &= \exp(-\beta^d \cdot z), \\ T^B &= \exp(-\beta^b \cdot z), \end{aligned} \quad (4)$$

where  $\beta^d$  and  $\beta^b$  are two RGB channel-wise medium coefficients, and  $z$  is the distance. In conjunction with Equation 3, we infer that as an object moves further from the camera, its color (direct signal) fades while the background light (backscatter signal) increasingly dominates. Assuming the background light is ideally uniform, the color transition in areas far from the camera in underwater scenes is smooth, leading to color distortion and low contrast. As described in Mini-splatting [12], this issue can undermine the effectiveness of adaptive density control used in the original 3DGS, which will be discussed in subsection 3.4. Consequently, only a limited number of sparse Gaussians are responsible for representing these regions, which often results in noticeable blur artifacts. Such issues are prevalent due to light absorption in underwater scenes. Therefore, we propose a new color appearance model and a physical-based density control module in UW-GS.

Moreover, moving objects such as fish and floating particles pose challenges to underwater 3D reconstruction. Their changing positions over time can cause errors in the appearance of static objects and introduce floaters in the rendering of novel views. Recent studies [31, 44, 48] have utilized temporal information to achieve 4D rendering; however, these methods typically model foreground motions with predictable motion trajectory and small displacements. In underwater environments, moving objects often exhibit fast speeds and significant positional changes, making dynamic rendering methods less suitable. Inspired by [35, 53],

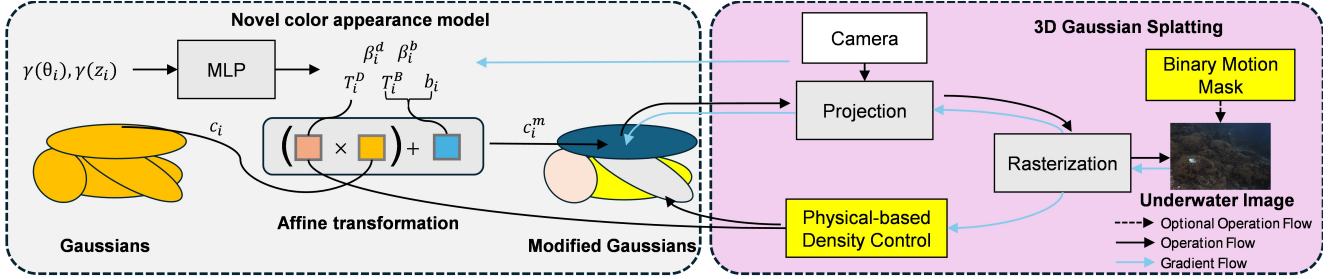


Figure 2. The diagram of our proposed UW-GS approach, combining a novel color appearance model, physical-based density control and binary motion mask to 3DGS. Our color appearance model uses view-direction  $R$  and depth  $z$  encoded by position encoding  $\gamma$  to estimate water condition parameters: attenuation factor  $T_i^D$ , backscatter factors  $T_i^B$ , and medium coefficients  $\beta_i^d$ ,  $\beta_i^b$  and  $b_i$ . In the splatting process, the physical-based density control module addresses densification failures and the binary motion mask handle distractors.

we propose a pixel-level mask, named Binary Motion Mask (BMM), which detects outlier objects and eliminate them from the scene.

### 3.2. Overview of UW-GS

The diagram of our UW-GS method is illustrated in [Figure 2](#), where our color appearance model is integrated into the 3DGS modified for underwater environments. The color appearance model using encoded depth and view direction as input for a multilayer perceptron (MLP) to estimate the parameters of the water medium and adjust the color of the Gaussian accordingly using an affine transformation. The 3D Gaussians with modified color will be sent to do 2D projection and then generate pixel color in rasterization module to output the final underwater image. The 3DGS includes a novel physics-based density control module using water medium estimation of MLP and a Binary Motion Mask (BMM) during training to mitigate the negative effects of the water medium and to handle moving objects, respectively.

### 3.3. Color Appearance Model

The original Gaussian color appearance in 3DGS [22] is derived from SHs, which assumes the scene medium is transparent and struggles to model varying attenuation and backscattering effects in water. To address this issue, we propose a novel approach for color appearance formation. The left panel of [Figure 2](#) illustrates the workflow of our method. Similar to [25], we use an additional MLP  $f$  with position encoded depth and viewing direction input to estimate medium properties:

$$(T_i^D, T_i^B, \beta_i^d, \beta_i^b, b_i) = f(\gamma(z_i), \gamma(\theta_i)), \quad i \in [1, N]. \quad (5)$$

Here  $z_i$  and  $\theta_i$  refer to the depth and view direction of Gaussian, respectively. We represent these by measuring the length and the normal vector of the line connecting the centers of the Gaussian and the camera. By using five head layers after the backbone, we can estimate the attenuation

and backscatter factors  $T_i^D$  and  $T_i^B$ , as well as medium coefficient per Gaussian:  $\beta_i^d$ ,  $\beta_i^b$  and  $b_i$ . These coefficients regulate two previous factors based on the physical model. Using the parameters obtained, the revised color  $c^m$  is then calculated by applying an affine transformation as follows:

$$c_i^m = T_i^D \cdot c_i + (1 - T_i^B) \cdot b_i, \quad (6)$$

This model enables us to adjust object appearance to model visibility that varies with distance in underwater scene. The modified color for Gaussians is then sent to 3DGS module.

### 3.4. Physical-based Density Control

In the standard 3DGS framework, the Gaussian point cloud is densified adaptively to acquire better representation capability. The 3DGS employs 2D position gradient  $\frac{\delta L_{Rec}}{\delta \text{mean}_{2D}}$ , which is derived from pixel color gradients  $\frac{\delta L_{Rec}}{\delta \text{color}}$ . If this gradient exceeds a threshold  $\tau$ , the Gaussian is split or cloned. However, in underwater scenes, [Equation 3](#) suggests that  $\frac{\delta L_{Rec}}{\delta \text{color}}$  is calculated from  $T^D \cdot \frac{\delta L_{Rec}}{\delta \text{color}^{object}}$  so that each Gaussian color gradient has an attenuation factor  $T^D$  due to light absorption effects. As shown in the left block in [Figure 3](#), the attenuation of the color gradient will result in the biased 2D position gradient calculation; we represent this effect as a function  $\alpha_{atten}(z)$ . Similar to  $T^D$ , this function is inverse correlated with depth  $z$ , meaning in underwater scenes, the 2D position gradient will diminish with distance. As a result, Gaussians can hardly be split or cloned in the far regions, leading to densification failures. This issue causes the blur artifact mentioned previously because of the sparse Gaussian distribution as shown in the right block of [Figure 3](#).

To mitigate the impact of the attenuation factor on gradient calculations, we introduce a refined densification strategy termed physics-based density control. For 2D position position gradient calculation, this approach employs the inverse of the estimated attenuation factor from novel appearance color model  $\frac{1}{T^D}$  to the underwater color gradient modeled as  $T^D \cdot \frac{\delta L_{Rec}}{\delta \text{color}^{object}}$ . Therefore, our  $\frac{\delta L_{Rec}}{\delta \text{color}} =$

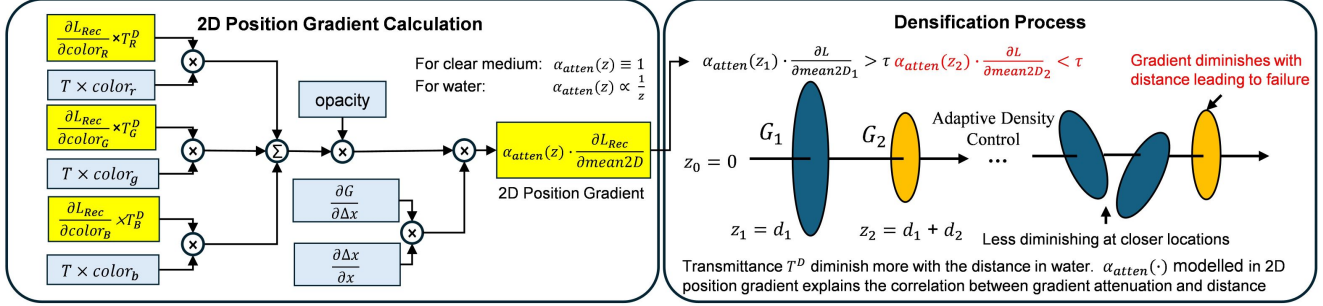


Figure 3. Left: Diagram of 2D Position gradient calculation. Right: Illustration of densification failures ( $G_2$  highlighted in orange) that appear to be not cloned or split in underwater scenes. Please Note  $color_{R,G,B}$  refers to color in pixel level while  $color_{r,g,b}$  represents Gaussian color derived from SHs, which is considered as object color.  $T$  refers to  $\prod_{j=1}^{i-1} (1 - \alpha_j)$  in Equation 2 for  $G_i$ .

$\frac{\delta L_{Rec}}{\delta color_{object}}$ . This adjustment effectively compensates for biased 2D position gradient calculations, allowing 3DGS to generate denser Gaussian point clouds with improved representational accuracy. Furthermore, by adjusting the 2D position gradient, this method optimizes regions where object color information is substantially attenuated, thereby enhancing 3DGS performance in areas characterized by smooth color transitions.

To further address the blur artifacts caused by large-size Gaussian projections, we follow [52] and consider the number of pixels covered in 2D space, rather than relying solely on view count to calculate average 2D position gradients for density control. This allows areas that were previously represented by sparse Gaussians in vanilla 3DGS to grow more effectively. As a result, the point clouds at larger scales exhibit improved representational capability, thereby reducing both blur and needle-like artifacts.

Additionally, to deal with floaters close to the camera, which is a common issue of 3DGS, inspired by [52], we typically reduce the 2D position gradients for Gaussians with a scaling factor  $S_z$  related to depth  $z$ . Hence, our final pixel color gradients are that  $\frac{\delta L_{Rec}}{\delta color} = S_z \frac{\delta L_{Rec}}{\delta color_{object}}$ . Combined with our physics-based density control, which scales gradients globally, this helps to suppress floaters near the camera without affecting our enhancement in other regions.

### 3.5. Binary Motion Mask

Although adopting the refined appearance model improves the modeling of underwater scenes, handling dynamic content in the dataset remains challenging. Some studies, such as [2, 19], have modeled moving objects by incorporating an additional time dimension. However, moving underwater content, such as fish and flickers, typically exhibits random trajectories and high speeds. Dynamic scene rendering algorithms that use a deformation field network are neither efficient nor effective in these cases.

Inspired by RobustNeRF [35], we introduce a Binary Motion Mask (BMM)  $\omega$  into our reconstruction loss func-

tion to eliminate the distractors as follows:

$$L_{Rec} = \lambda \cdot \omega \cdot L_1 + (1 - \lambda) \cdot \omega \cdot L_{D-SSIM}, \quad (7)$$

where  $\lambda$  is a loss weight.

As indicated in [35], the trimmed estimator is very effective in detecting a portion of the outliers in the set. In our implementation,  $\omega_t$  at the iteration of  $t$  is computed as follows:

$$\omega_1^t = \epsilon^t \leq T_\epsilon, \quad (8)$$

where  $\epsilon^t$  is a residual, computing from  $\epsilon^t = \|\hat{I}_t - I\|_2$ , and  $\hat{I}_t$  is the rendered image at the iteration  $t$ .

In Equation 8, we hypothesize that residuals below the a threshold  $T_\epsilon$ , set by dividing sorted residuals from the previous iteration, belong to the inliers, while the rest are considered outliers. However, relying solely on this mask is insufficient to effectively distinguish distractors, which may introduce distortion in our rendering. For this reason, a  $3 \times 3$  diffusion kernel  $B$  is applied to maintain spatial smoothness as shown in Equation 9. Moreover, to avoid high-frequency content being treated as outliers, every  $8 \times 8$  patch  $R_{8 \times 8}$  is classified according to the average value of its  $16 \times 16$  neighbors  $R_{16 \times 16}$ . The third mask is then described as shown in Equation 10.

$$\omega_2^t = \omega_1^t * B \geq T_*, \quad (9)$$

$$\omega_3^t(R_{8 \times 8}) = \overline{\omega_2^t(R_{16 \times 16})} \geq T_R, \quad (10)$$

where  $T_*$  and  $T_R$  are thresholds and can be manually tuned like  $T_\epsilon$ . If a pixel is classified as an inlier by any of the three weighting formulas described above, it is ultimately regarded as an inlier to prevent our estimation from being overly aggressive. The final BMM at  $t$  is then obtained from

$$\omega^t = \omega_1^t \cup \omega_2^t \cup \omega_3^t. \quad (11)$$

### 3.6. Loss Function

The final loss function,  $\mathcal{L}$ , used for optimization, comprises a reconstruction loss  $L_{Rec}$  (see subsection 3.5), a

depth-supervised loss  $L_{da}$ , and a gray-world assumption loss  $L_g$ , defined as follows:

$$\mathcal{L} = L_{Rec} + L_{da} + L_g. \quad (12)$$

**Depth-supervised loss  $L_{da}$ .** Depth information is the key to underwater scene modeling. In 3DGS, we can render depth maps in a similar way as image:

$$\hat{D} = \sum_{i \in N} \alpha_i z_i \prod_{j=1}^{i-1} (1 - \alpha_j). \quad (13)$$

However, unreasonable positioned Gaussian sets, such as floaters, will heavily affect our estimation of the underwater medium coefficients due to the erroneous depth measurements. In order to enhance the reliability of the depth measurements between the Gaussians mean center and the camera center and diminish the floater issue. We implement a depth-supervised loss, denoted as  $L_{da}$ :

$$L_{da} = \lambda_d L_d + \lambda_{ca} L_{ca},$$

$$L_d = \|\hat{D} - D\|, \quad L_{ca} = \sum_{x \in \{r,g,b\}} \sum_{y \in \{d,b\}} \|\hat{z}_x^y - z\|, \quad (14)$$

where  $\lambda_d$  and  $\lambda_{ca}$  are hyperparameters, and  $L_d$  is a depth supervision L1 loss. We use a synthetic ground truth depth map  $D$  that is predicted by DepthAnything [47], a novel monocular depth estimation model that can adapt to any environment. Please note Both  $D$  and  $\hat{D}$  are normalized to aligned relatively instead of absolutely. Inspired by [40],  $L_{ca}$ , named channel-wise depth alignment loss is also included. This loss is developed based on the underwater image formation model Equation 3, resulting in the approximate depth per Gaussian can be calculated in the other way:  $\hat{z}_x^y = -\frac{\log(T_x^y)}{\beta^y}$ .  $z$  is the measured depth of the Gaussian.  $L_{ca}$  imposes restrictions on  $T^D$  and  $T^B$ , which are closely related to the depth. Here in  $L_{da}$ , we correct depth information at both the pixel and Gaussian point levels.

**Gray-world assumption loss  $L_g$ .** A gray-world assumption loss  $L_g$  based on the image restoration prior knowledge [13] is also incorporated:

$$L_g = \sum_{x \in \{r,g,b\}} \|\mu(J^x) - 0.5\|_2^2. \quad (15)$$

Grounded in the Gray-world assumption,  $L_g$  serves to constrain the color of objects within the scene that have similar average values across the RGB channels, with the objective of ensuring that  $\beta^d$ ,  $\beta^b$  and  $b$  are predicted in an appropriate manner.

## 4. Experiment Configuration

**Datasets.** Three datasets were used for performance evaluation: i) SeaThru-NeRF [26]; ii) the in-the-wild (IW)

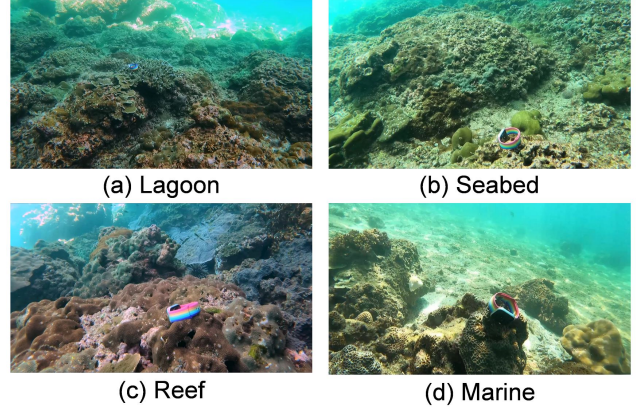


Figure 4. Sample images from S-UW dataset.

dataset from [39], and iii) our dataset, S-UW. SeaThru-NeRF [26] comprises four image sequences captured in different seas, each pre-processed with white balance enhancement to reduce noise. The IW dataset [39] was captured at mid-depth underwater, with moving object masks available. This dataset was used for evaluating the BMM performance.

Our S-UW dataset consists of high-definition underwater videos across four larger areas scenarios, each containing 24 images. Examples of these scenes are shown in Figure 4. Unlike existing datasets, S-UW was captured in shallow waters and introduces additional challenges, such as flickering. For all videos, we selected one image out of every eight images for testing.

**Implementation Details.** Our method is implemented using Pytorch. We utilized COLMAP [36] to initialize the point cloud and estimate the camera position of the images in the sequence. We modified the diff-gaussian-rasterization used in original 3DGS to render depth maps, incorporating the additional gradient calculation branch in a backward process for depth loss. For the medium MLP, we use two linear layers with 64 features and additional head layers for each output. Softplus activation is adopted for  $\beta^D$  and  $\beta^B$  while Sigmoid is used for  $T^D$ ,  $T^B$  and  $b$ .

For training, we carried out 15,000 iterations in a single RTX3090 GPU. The first 1,000 iterations are used as a warm-up phase, in which we optimize the model by solely using depth loss  $L_d$  and depth-supervised loss  $L_{da}$  to adjust the initialized point cloud and pre-train MLP. Subsequently, we used the same optimization setting as the original 3DGS to optimize Gaussian attributes and applied an independent Adam optimizer to train our medium MLP. The BMM, is applied to the scenes containing dynamic objects.

**Baselines and Metrics.** We tested our method and compared with three state of the arts: Instant-NGP [33], SeaThru-NeRF [26], and original 3DGS [22]. We used their official implementation, but trained on the same sequence using the same dataset split strategy. We computed

SeaThru-NeRF												
Scene Method	Curacao			Panama			IUI-Reasea			Japanese-Reasea		
	PSNR $\uparrow$	SSIM $\uparrow$	LPIPS $\downarrow$	PSNR $\uparrow$	SSIM $\uparrow$	LPIPS $\downarrow$	PSNR $\uparrow$	SSIM $\uparrow$	LPIPS $\downarrow$	PSNR $\uparrow$	SSIM $\uparrow$	LPIPS $\downarrow$
Instant-NGP [33]	27.9051	0.7069	0.3853	23.4593	0.6359	0.4262	20.6342	0.5577	0.6027	<b>23.2302</b>	0.6551	0.3567
SeaThru-NeRF [26]	29.9210	0.8563	0.2976	26.9008	0.7893	0.3297	<u>25.8899</u>	0.7537	0.3534	21.7473	0.7351	0.3367
3DGS [22]	<u>30.9733</u>	<u>0.9356</u>	<u>0.1930</u>	<u>30.8030</u>	<u>0.9186</u>	<u>0.1963</u>	23.1343	<u>0.8774</u>	<u>0.2402</u>	21.9711	<b>0.8671</b>	<u>0.2018</u>
UW-GS (ours)	<b>31.7714</b>	<b>0.9430</b>	<b>0.1441</b>	<b>31.7902</b>	<b>0.9360</b>	<b>0.1156</b>	<b>28.6523</b>	<b>0.9334</b>	<b>0.1252</b>	<u>23.0465</u>	<u>0.8602</u>	<b>0.1899</b>

S-UW												
Scene Method	Lagoon			Seabed			Reef			Marine		
	PSNR $\uparrow$	SSIM $\uparrow$	LPIPS $\downarrow$	PSNR $\uparrow$	SSIM $\uparrow$	LPIPS $\downarrow$	PSNR $\uparrow$	SSIM $\uparrow$	LPIPS $\downarrow$	PSNR $\uparrow$	SSIM $\uparrow$	LPIPS $\downarrow$
Instant-NGP [33]	21.6674	0.5480	0.3198	19.6167	0.4275	0.3198	18.5866	0.4382	0.5058	15.7300	0.4637	0.4410
SeaThru-NeRF [26]	25.5424	0.7592	0.2860	22.7050	0.6407	0.3455	18.5510	0.4077	0.5522	18.1031	0.5718	0.4582
3DGS [22]	<b>27.1166</b>	<u>0.8707</u>	<u>0.1606</u>	<u>26.4933</u>	<b>0.8234</b>	<u>0.1684</u>	<u>22.4663</u>	<u>0.7117</u>	<u>0.2646</u>	<u>18.9492</u>	<u>0.6922</u>	<u>0.2990</u>
UW-GS (ours)	<u>26.9103</u>	<b>0.8736</b>	<b>0.1479</b>	<b>26.5088</b>	<u>0.8197</u>	<b>0.1541</b>	<b>23.3078</b>	<b>0.7277</b>	<b>0.2504</b>	<b>20.0065</b>	<b>0.7145</b>	<b>0.2678</b>

Table 1. Qualitative results of the proposed method evaluated on SeaThru-NeRF and S-UW dataset.  $\uparrow$  refers larger values are better while  $\downarrow$  is opposite. **Bold** indicates the best results and underline values represent the second best.

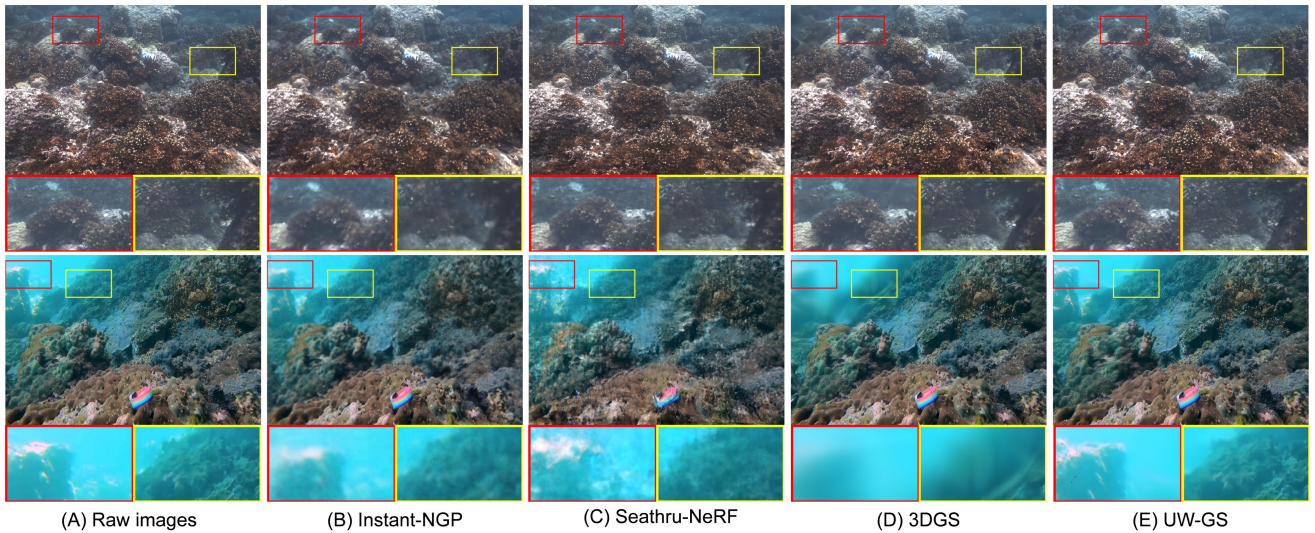


Figure 5. Novel view rendering comparison in **Panama** from Seathru-NeRF dataset [26] and **Reef** from S-UW. We have shown details below the images. Please note that images in first row are enhanced for visualization.

the global PSNR, SSIM and LPIPS values in the static areas. On the other hand, we will also use these three metrics in dynamic scenes after using motion mask provided from dataset to exclude moving objects.

## 5. Results and Discussion

**Quantitative results.** Table 1 shows the evaluation results of the SeaThru-NeRF and S-UW datasets for the rendered quality of each benchmark. For the SeaThru-NeRF dataset, our method shows the best overall performance and achieves average 2.09dB and 2.70dB PSNR improvement compared to 3DGS and Seathru-NeRF respectively, although it has the second-best SSIM in the Japanese-RedSea scene. For the S-UW dataset, while UW-GS ranks second in PSNR for the Lagoon and in SSIM for the Seabed

scene, it still performs best and exceeds the average PSNR of 3DGS and Seathru-NeRF by 0.43 dB and 2.96 dB, respectively. The limited improvement compared to 3DGS can be attributed to the unstable lighting from above the water surface.

**Qualitative results.** Figure 5 presents a visual comparison between the baseline methods and UW-GS. The first row shows the results for the SeaThru-NeRF dataset, while the second row displays the results for the S-UW dataset. In summary, our method enhances the quality of novel view synthesis results with better reconstruction of distant regions and fewer artifacts. Our approach illustrates effectiveness and robustness across various scenes.

In addition, our method demonstrates its capability to distinguish objects from the scattering medium. In this context, we attempted to “drain” the water to present clearer



Figure 6. The first row present render images while the second row shows their corresponding estimated clean images  $\hat{J}$ , which are obtained by solely use color of Gaussian in rasterization without transformation. From left to right come from **Japanese-Redsea**, **Lagoon** and **Curasao** scene respectively.



Figure 7. Examples of rendering results from **Composite** and **Sardine** scenes. From left to right: raw videos, results without and with BMM, respectively.

restored results based on the estimated water medium acquired from our model. Figure 6 shows that our method has potential in the enhancement of underwater scenes.

**Ablation study.** We isolate our contributions using a set of modified architectures: (V1) solely using spherical harmonics to represent view-dependent color (note that MLP will also assist with density control), (V2) training UW-GS without physics-based density control, and (V3) removing the depth-supervised loss. The results are shown in Table 2 verifies that our architecture can achieve the overall best performance while others suffer from performance degradation.

We also analyzed how the three masks used in the BMM contribute to moving object removal. We selected two challenging scenes from the IW dataset [39], which includes motion masks that aid in assessing reconstruction quality by excluding dynamic content. Table 3 indicates our method yields the best performance. Demonstrate BMM combining three masks can best retain static content during training.

**Limitations.** The improvement of our method is not obvious in the shallow underwater scene because the disturbance of light from above the water cannot be neglected. Subjectively, our method eliminates dynamic distractors

Configuration	PSNR $\uparrow$	SSIM $\uparrow$	LPIPS $\downarrow$
V1	25.4132	0.8338	0.1884
V2	25.9165	0.8313	0.2115
V3	25.7046	0.8392	0.2026
Ours	<b>26.4982</b>	<b>0.8510</b>	<b>0.1744</b>

Table 2. Ablation Study on SeaThru-NeRF and S-UW Scenes using our proposed methods and its modified architectures

BMM Break Down			
Configuration	PSNR $\uparrow$	SSIM $\downarrow$	LPIPS $\downarrow$
+ $\omega_1$	24.1491	0.8568	0.1625
+ $\omega_2$	24.6537	0.8943	0.1251
+ $\omega_3$ (Ours)	<b>25.9267</b>	<b>0.9081</b>	<b>0.1098</b>

Table 3. Performance on different marks in BMM, training in **Composite** and **Sardine** scenes [39]. Motion masks are provided with the dataset.

method	PSNR	SSIM	LPIPS
UW-GS without BMM	27.8302	0.9231	0.0960
UW-GS using BMM	25.9267	0.9081	0.1098

Table 4. The average results of **Composite** and **Sardine** scenes [39] using and without a BMM during training.

from scene renderings without any additional pre- or post-processing. More subjective results are included in supplementary materials. However, because BMM may imperfectly classify, the reconstruction quality in static areas is somewhat degraded, as seen in the objective results of IW dataset shown in Table 4.

## 6. Conclusion

This paper presents a novel 3DGS-based method for underwater applications. We introduce a novel color appearance model to better represent distance-dependent attenuation and backscatter, which significantly enhances reconstruction results, especially in far regions strongly influenced by water effects. Additionally, we propose the BMM that effectively eliminate the shadow-like artifacts due to the distractors by excluding them during the training. We also introduce a challenging underwater dataset, comprising 4 different scenes. Our method is tested on several scenes from three datasets and outperforms the existing static underwater scene reconstruction baselines while demonstrating the ability to handle dynamics, highlighting its promising potential for underwater environment exploration and research.

## References

- [1] Derya Akkaynak and Tali Treibitz. A revised underwater image formation model. In *the IEEE/CVF Conference on Computer Vision and Pattern Recognition (CVPR)*, pages 6723–6732, 2018. 2, 3
- [2] A. Azzarelli, N. Anantrasirchai, and D. R. Bull. Waveplanes: A compact wavelet representation for dynamic neural radiance fields. *arXiv preprint arXiv:2312.02218*, 2023. 5
- [3] Jonathan T Barron, Ben Mildenhall, Matthew Tancik, Peter Hedman, Ricardo Martin-Brualla, and Pratul P Srinivasan. Mip-nerf: A multiscale representation for anti-aliasing neural radiance fields. In *International Conference on Computer Vision (ICCV)*, pages 5855–5864, 2021. 2
- [4] Jonathan T Barron, Ben Mildenhall, Dor Verbin, Pratul P Srinivasan, and Peter Hedman. Mip-nerf 360: Unbounded anti-aliased neural radiance fields. In *the IEEE/CVF Conference on Computer Vision and Pattern Recognition (CVPR)*, pages 5470–5479, 2022. 2
- [5] Jonathan T Barron, Ben Mildenhall, Dor Verbin, Pratul P Srinivasan, and Peter Hedman. Zip-nerf: Anti-aliased grid-based neural radiance fields. In *International Conference on Computer Vision (ICCV)*, pages 19697–19705, 2023. 2
- [6] Guikun Chen and Wenguan Wang. A survey on 3d gaussian splatting. *arXiv preprint arXiv:2401.03890*, 2024. 1
- [7] Wenbo Chen and Ligang Liu. Deblur-gs: 3d gaussian splatting from camera motion blurred images. *Proceedings of the ACM on Computer Graphics and Interactive Techniques*, 7(1):1–15, 2024. 3
- [8] V Croce, G Caroti, L De Luca, A Piemonte, and P Véron. Neural radiance fields (nerf): Review and potential applications to digital cultural heritage. *The International Archives of the Photogrammetry, Remote Sensing and Spatial Information Sciences*, 48:453–460, 2023. 2
- [9] Arnold G Dekker, Vittorio E Brando, Janet M Anstee, Nicole Pinnel, Tiit Kutser, Erin J Hoogenboom, Steef Peters, Reinold Pasterkamp, Robert Vos, Carsten Olbert, et al. Imaging spectrometry of water. *Imaging spectrometry: Basic principles and prospective applications*, pages 307–359, 2001. 2
- [10] Philip Dutre, Philippe Bekaert, and Kavita Bala. *Advanced global illumination*. AK Peters/CRC Press, 2018. 2
- [11] Marc Ebner. Color constancy based on local space average color. *Machine Vision and Applications*, 20(5):283–301, 2009. 2
- [12] Guangchi Fang and Bing Wang. Mini-splatting: Representing scenes with a constrained number of gaussians. *arXiv preprint arXiv:2403.14166*, 2024. 3
- [13] Zhenqi Fu, Huangxing Lin, Yan Yang, Shu Chai, Liyan Sun, Yue Huang, and Xinghao Ding. Unsupervised underwater image restoration: From a homology perspective. In *Proceedings of the AAAI Conference on Artificial Intelligence (AAAI)*, volume 36, pages 643–651, 2022. 6
- [14] Xiangjun Gao, Xiaoyu Li, Yiyu Zhuang, Qi Zhang, Wenbo Hu, Chaopeng Zhang, Yao Yao, Ying Shan, and Long Quan. Mani-gs: Gaussian splatting manipulation with triangular mesh. *arXiv preprint arXiv:2405.17811*, 2024. 1
- [15] Rafael C Gonzalez. *Digital image processing*. Pearson education india, 2009. 2
- [16] Salma P González-Sabbagh and Antonio Robles-Kelly. A survey on underwater computer vision. *ACM Computing Surveys*, 55(13s):1–39, 2023. 2
- [17] Kaiming He, Jian Sun, and Xiaoou Tang. Single image haze removal using dark channel prior. *IEEE transactions on pattern analysis and machine intelligence*, 33(12):2341–2353, 2010. 2
- [18] Xudong Huang, Wei Li, Jie Hu, Hanting Chen, and Yunhe Wang. Refsr-nerf: Towards high fidelity and super resolution view synthesis. In *the IEEE/CVF Conference on Computer Vision and Pattern Recognition (CVPR)*, pages 8244–8253, 2023. 2
- [19] Yi-Hua Huang, Yang-Tian Sun, Ziyi Yang, Xiaoyang Lyu, Yan-Pei Cao, and Xiaojuan Qi. Sc-gs: Sparse-controlled gaussian splatting for editable dynamic scenes. In *the IEEE/CVF Conference on Computer Vision and Pattern Recognition (CVPR)*, pages 4220–4230, 2024. 5
- [20] Fushuo Huo, Bingheng Li, and Xuegui Zhu. Efficient wavelet boost learning-based multi-stage progressive refinement network for underwater image enhancement. In *International Conference on Computer Vision (ICCV)*, pages 1944–1952, 2021. 2
- [21] Aupendu Kar, Sobhan Kanti Dhara, Debashis Sen, and Prabir Kumar Biswas. Zero-shot single image restoration through controlled perturbation of koschmieder’s model. In *the IEEE/CVF Conference on Computer Vision and Pattern Recognition (CVPR)*, pages 16205–16215, 2021. 2
- [22] Bernhard Kerbl, Georgios Kopanas, Thomas Leimkühler, and George Drettakis. 3d gaussian splatting for real-time radiance field rendering. *ACM Trans. Graph.*, 42(4):139–1, 2023. 1, 2, 3, 4, 6, 7
- [23] Sieun Kim, Kyungjin Lee, and Youngki Lee. Color-cued efficient densification method for 3d gaussian splatting. In *the IEEE/CVF Conference on Computer Vision and Pattern Recognition (CVPR)*, pages 775–783, 2024. 3
- [24] Byeonghyeon Lee, Howoong Lee, Xiangyu Sun, Usman Ali, and Eunbyung Park. Deblurring 3d gaussian splatting. *arXiv preprint arXiv:2401.00834*, 2024. 3
- [25] Joo Chan Lee, Daniel Rho, Xiangyu Sun, Jong Hwan Ko, and Eunbyung Park. Compact 3d gaussian representation for radiance field. In *the IEEE/CVF Conference on Computer Vision and Pattern Recognition (CVPR)*, pages 21719–21728, 2024. 4
- [26] Deborah Levy, Amit Peleg, Naama Pearl, Dan Rosenbaum, Derya Akkaynak, Simon Korman, and Tali Treibitz. Seathru-nerf: Neural radiance fields in scattering media. In *the IEEE/CVF Conference on Computer Vision and Pattern Recognition (CVPR)*, pages 56–65, 2023. 1, 3, 6, 7
- [27] Huapeng Li, Wenxuan Song, Tianao Xu, Alexandre Elsig, and Jonas Kulhanek. Watersplattling: Fast underwater 3d scene reconstruction using gaussian splatting. *arXiv preprint arXiv:2408.08206*, 2024. 3
- [28] Quewei Li, Feichao Li, Jie Guo, and Yanwen Guo. Uhd-nerf: Ultra-high-definition neural radiance fields. In *International Conference on Computer Vision (ICCV)*, pages 23097–23108, 2023. 2

- [29] Ruilong Li, Hang Gao, Matthew Tancik, and Angjoo Kanazawa. Nerfacc: Efficient sampling accelerates nerfs. In *International Conference on Computer Vision (ICCV)*, pages 18537–18546, 2023. 3
- [30] Zhengqi Li, Simon Niklaus, Noah Snavely, and Oliver Wang. Neural scene flow fields for space-time view synthesis of dynamic scenes. In *the IEEE/CVF Conference on Computer Vision and Pattern Recognition (CVPR)*, pages 6498–6508, 2021. 3
- [31] Youtian Lin, Zuozhuo Dai, Siyu Zhu, and Yao Yao. Gaussian-flow: 4d reconstruction with dynamic 3d gaussian particle. In *the IEEE/CVF Conference on Computer Vision and Pattern Recognition (CVPR)*, pages 21136–21145, 2024. 3
- [32] Ben Mildenhall, Pratul P. Srinivasan, Matthew Tancik, Jonathan T. Barron, Ravi Ramamoorthi, and Ren Ng. Nerf: Representing scenes as neural radiance fields for view synthesis. In *Proceedings of the European Conference on Computer Vision (ECCV)*, pages 405–421, 2020. 1, 2
- [33] Thomas Müller, Alex Evans, Christoph Schied, and Alexander Keller. Instant neural graphics primitives with a multi-resolution hash encoding. *ACM transactions on graphics (TOG)*, 41(4):1–15, 2022. 6, 7
- [34] Andrea Ramazzina, Mario Bijelic, Stefanie Walz, Alessandro Sanvito, Dominik Scheuble, and Felix Heide. Scatternerf: Seeing through fog with physically-based inverse neural rendering. In *International Conference on Computer Vision (ICCV)*, pages 17957–17968, 2023. 1, 3
- [35] Sara Sabour, Suhani Vora, Daniel Duckworth, Ivan Krasin, David J Fleet, and Andrea Tagliasacchi. Robustnerf: Ignoring distractors with robust losses. In *the IEEE/CVF Conference on Computer Vision and Pattern Recognition (CVPR)*, pages 20626–20636, 2023. 1, 3, 5
- [36] Johannes L Schonberger and Jan-Michael Frahm. Structure-from-motion revisited. In *the IEEE/CVF Conference on Computer Vision and Pattern Recognition (CVPR)*, pages 4104–4113, 2016. 3, 6
- [37] Nagabhushan Somraj and Rajiv Soundararajan. Vip-nerf: Visibility prior for sparse input neural radiance fields. In *ACM SIGGRAPH 2023 Conference Proceedings*, pages 1–11, 2023. 3
- [38] Jiaxiang Tang, Hang Zhou, Xiaokang Chen, Tianshu Hu, Er-rui Ding, Jingdong Wang, and Gang Zeng. Delicate textured mesh recovery from nerf via adaptive surface refinement. In *International Conference on Computer Vision (ICCV)*, pages 17739–17749, 2023. 2
- [39] Yunkai Tang, Chengxuan Zhu, Renjie Wan, Chao Xu, and Boxin Shi. Neural underwater scene representation. In *the IEEE/CVF Conference on Computer Vision and Pattern Recognition (CVPR)*, pages 11780–11789, 2024. 1, 3, 6, 8
- [40] Nisha Varghese, Ashish Kumar, and AN Rajagopalan. Self-supervised monocular underwater depth recovery, image restoration, and a real-sea video dataset. In *International Conference on Computer Vision (ICCV)*, pages 12248–12258, 2023. 6
- [41] Peng Wang, Yuan Liu, Zhaoxi Chen, Lingjie Liu, Ziwei Liu, Taku Komura, Christian Theobalt, and Wenping Wang. F2-nerf: Fast neural radiance field training with free camera trajectories. In *the IEEE/CVF Conference on Computer Vision and Pattern Recognition (CVPR)*, pages 4150–4159, 2023. 2
- [42] Peng Wang, Lingzhe Zhao, Ruijie Ma, and Peidong Liu. Bad-nerf: Bundle adjusted deblur neural radiance fields. In *the IEEE/CVF Conference on Computer Vision and Pattern Recognition (CVPR)*, pages 4170–4179, 2023. 2
- [43] Guanjun Wu, Taoran Yi, Jiemin Fang, Lingxi Xie, Xiaopeng Zhang, Wei Wei, Wenyu Liu, Qi Tian, and Xinggang Wang. 4d gaussian splatting for real-time dynamic scene rendering. In *the IEEE/CVF Conference on Computer Vision and Pattern Recognition (CVPR)*, pages 20310–20320, 2024. 3
- [44] Guanjun Wu, Taoran Yi, Jiemin Fang, Lingxi Xie, Xiaopeng Zhang, Wei Wei, Wenyu Liu, Qi Tian, and Xinggang Wang. 4d gaussian splatting for real-time dynamic scene rendering. In *the IEEE/CVF Conference on Computer Vision and Pattern Recognition (CVPR)*, pages 20310–20320, 2024. 3
- [45] Xiufeng Xie, Riccardo Gherardi, Zhihong Pan, and Stephen Huang. Hollownerf: Pruning hashgrid-based nerfs with trainable collision mitigation. In *International Conference on Computer Vision (ICCV)*, pages 3480–3490, 2023. 2
- [46] Zhiwen Yan, Weng Fei Low, Yu Chen, and Gim Hee Lee. Multi-scale 3d gaussian splatting for anti-aliased rendering. In *the IEEE/CVF Conference on Computer Vision and Pattern Recognition (CVPR)*, pages 20923–20931, 2024. 3
- [47] Lihe Yang, Bingyi Kang, Zilong Huang, Xiaogang Xu, Jiashi Feng, and Hengshuang Zhao. Depth anything: Unleashing the power of large-scale unlabeled data. In *the IEEE/CVF Conference on Computer Vision and Pattern Recognition (CVPR)*, pages 10371–10381, 2024. 2, 6
- [48] Ziyi Yang, Xinyu Gao, Wen Zhou, Shaohui Jiao, Yuqing Zhang, and Xiaogang Jin. Deformable 3d gaussians for high-fidelity monocular dynamic scene reconstruction. In *the IEEE/CVF Conference on Computer Vision and Pattern Recognition (CVPR)*, pages 20331–20341, 2024. 3
- [49] Zehao Yu, Anpei Chen, Binbin Huang, Torsten Sattler, and Andreas Geiger. Mip-splatting: Alias-free 3d gaussian splatting. In *the IEEE/CVF Conference on Computer Vision and Pattern Recognition (CVPR)*, pages 19447–19456, 2024. 3
- [50] Fan Zhang, Shaodi You, Yu Li, and Ying Fu. Atlantis: Enabling underwater depth estimation with stable diffusion. In *the IEEE/CVF Conference on Computer Vision and Pattern Recognition (CVPR)*, pages 11852–11861, 2024. 2
- [51] Jiahui Zhang, Fangneng Zhan, Muyu Xu, Shijian Lu, and Eric Xing. Fregs: 3d gaussian splatting with progressive frequency regularization. In *the IEEE/CVF Conference on Computer Vision and Pattern Recognition (CVPR)*, pages 21424–21433, 2024. 3
- [52] Zheng Zhang, Wenbo Hu, Yixing Lao, Tong He, and Hengshuang Zhao. Pixel-gs: Density control with pixel-aware gradient for 3d gaussian splatting. *arXiv preprint arXiv:2403.15530*, 2024. 3, 5
- [53] Xiaoyu Zhou, Zhiwei Lin, Xiaojuan Shan, Yongtao Wang, Deqing Sun, and Ming-Hsuan Yang. Drivinggaussian: Composite gaussian splatting for surrounding dynamic autonomous driving scenes. In *the IEEE/CVF Conference on Computer Vision and Pattern Recognition (CVPR)*, pages 21634–21643, 2024. 3